Proceedings of the 11th European Conference on Underwater Acoustics

WAVEGUIDE PROPERTIES OF ACTIVE INTENSITY VORTICITY

DR Dall'Osto Dept. of Mechanical Engineering and the Applied Physics Laboratory, University of Washington, Seattle, Washington, USA
PH Dahl Dept. of Mechanical Engineering and the Applied Physics Laboratory, University of Washington, Seattle, Washington, USA

1 INTRODUCTION

Measurement of the active intensity vorticity is possible by both particle motion sensors and by finite difference methods applied to closely spaced pressure measurements. In a shallow water waveguide, the reflections from the horizontal sea-surface and sea-floor create regions with elliptical particle motion paths; both the magnitude of these intensity components and the magnitude of the active intensity vorticity perpendicular to this plane determines the shape of the ellipse. Experimental measurements of the particle motion vector in shallow water confirms the observability of the active intensity vorticity (and elliptical particle motion) in the vertical plane [1].

This paper focuses on a set of experimental measurements of the vertical intensity from the 2006 Shallow Water Experiment (SW06). The paper is organized as follows. First, we introduce the concepts of active and reactive intensity in terms of a simple waveguide model. This is used to clarify the relationship between interference patterns and active intensity vorticity which is the curl of the active intensity vector. Time dependent simulations are used to discuss the active intensity vorticity with the ultimate goal of demonstrating how these vector properties can be observed by the vertical component of intensity. Next, experimental data is interpreted in terms of the vertical components of active and reactive intensity. Properties of the active intensity vorticity are analyzed together with numerical simulations using accepted and documented environmental models of the experimental area. This interpretation of pressure data reveals some waveguide properties not readily observable in the pressure magnitude. We show here that the nature of vector intensity can be exploited to determine environmental characteristics.

2 ACTIVE INTENSITY VORTICITY

The use of vorticity to describe a property of the acoustic field at first glance may seem inappropriate. Given that particle velocity can be represented as the gradient of a velocity potential, the vorticity (or curl) of the particle velocity field is zero [2]. However, a non-zero curl can occur in the complex intensity vector field,

$$\vec{I}_c = p\vec{v}^* \tag{1}$$

where p and $\vec{v}$ are the complex pressure and particle velocity vector respectively ($\vec{v}^*$ is the complex conjugate.) The active intensity is

$$\vec{I} = Re(\vec{I}_c), \tag{2}$$

and represents the propagating energy flux which can have a non-zero curl. The reactive intensity is

$$\vec{Q} = Im(\vec{I}_c) \tag{3}$$

and represents the portion of energy flux that, in a time-average sense, averages to zero. The curl of reactive intensity is always zero. Reactive intensity represents the non-propagating energy flux and is dependent on the degree to which the pressure and particle velocity are out of phase. When pressure and particle velocity are completely out of phase, the intensity field is completely reactive.

In the acoustic field of a point source in the free-field (no boundaries) the active intensity vorticity is zero. The complex intensity of a point source is directed outward from the source and is equal to $\frac{|p|^2}{\rho_0 c}(1 + i\frac{1}{kr})$, where ρ_0 is the density of the medium, r is the range from the source and k is the wavenumber $2\pi/\lambda$. A non-zero curl in the active intensity field occurs when the active and reactive intensity vectors point in different directions [3]. Both the active and reactive intensity vectors in the free-field point source model point radially outward from the source, and as they are in the same direction the active intensity vorticity is zero. The active and reactive intensity vector fields of a point source near a reflecting boundary, however, are not necessarily aligned. Here the interference from the reflection establishes an additional component of reactive intensity perpendicular to the reflection plane and the active intensity vorticity is non-zero.

2.1 ACTIVE INTENSITY VORTICITY FOR A NEAR SURFACE SOURCE

To illustrate the relationship between between the vorticity of active intensity and the particle motion, let us consider the interference of the direct arrival and surface reflection of a submerged source, a situation one would encounter in deep water measurements often referred to as Lloyd's mirror. Figure 1(a) shows the active intensity field of a steady tone (1000 Hz) from a point source 1.5 m below the sea-surface, computed here by the method of images. Figure 1(b) shows the range dependence of intensity magnitude and active intensity vorticity (scaled to their respective maximum values) at 20 m depth. In general, the active intensity is directed downward away from the surface, except in regions of strong destructive interference. As shown by the components of active intensity expanded in the inset of Fig. 1(b), at the minimum the vertical component is directed toward the sea-surface (the negative direction in this sign convention.)

Active intensity vorticity describes an important feature of the particle motion, specifically the elliptical particle motion caused by interfering wavefronts from reflecting boundaries. Shchurov, et al. [1] show that the curl of the active intensity vector relates to the magnitude and phase properties of the particle velocity components (the ellipticity of the particle motion.) For a tonal signal this curl is

$$\nabla \times \vec{I} = -2\omega\rho_0[v_y v_z \sin(\phi_y - \phi_z)\vec{x} + v_x v_z \sin(\phi_x - \phi_z)\vec{y} + v_y v_x \sin(\phi_y - \phi_x)\vec{z}] \qquad (4)$$

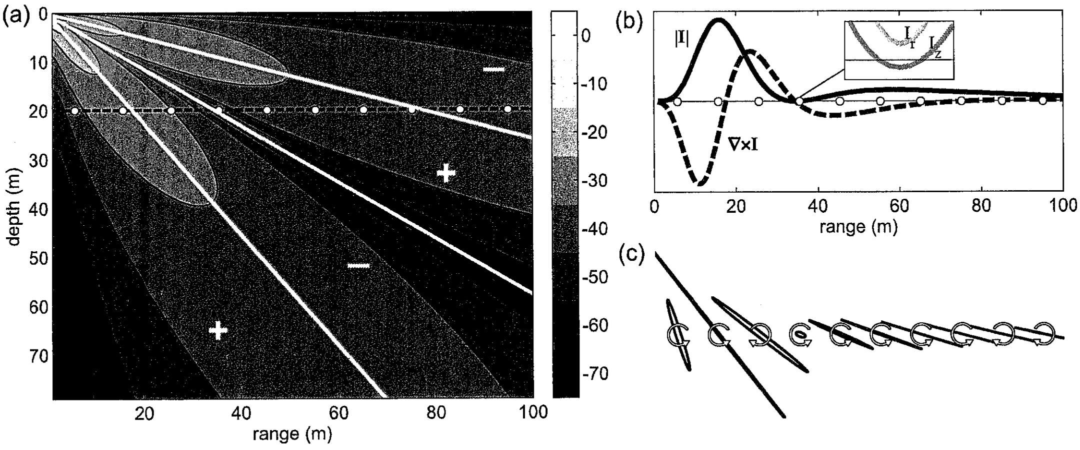

Figure 1: (a) Contours of the steady-state active intensity magnitude for a 1000 Hz source positioned 1.5 m below the sea-surface. Regions of (+/−) active intensity vorticity are separated by the white contour lines. (b) The active intensity vorticity and the active intensity magnitude corresponding to the horizontal cut at 20 m, the vertical and horizontal components near the minimum are shown in the inset. (c) The particle motion path and its direction/polarization for the white circles along the 20 m horizontal cut.

where ω is the angular frequency, and v_m and ϕ_m are the particle velocity magnitude and phase in the m-direction. Equation (4) states that the degree of ellipticity of the particle motion corresponds to the magnitude of the active intensity vorticity perpendicular to that plane. For example, when the two xy-plane components of the particle velocity vector are of equal magnitude but $90°$ out of phase, the particle motion follows a circular path and the active intensity vorticity in the z-direction is non-zero. In contrast, when the two velocity components are completely in phase, the particle motion follows a linear path and the active intensity vorticity is zero.

The sign of the active intensity vorticity indicates the particle motion polarization, a clockwise or counter-clockwise motion around the elliptical path. For a linear path, the polarization has no physical meaning, but here the active intensity vorticity is zero. The sign of the active intensity vorticity contains information relating to the reflection process and its interference pattern. Active intensity vorticity can be measured by applying Eq. 4 to the output of a particle motion sensor. Similarly, finite difference methods applied to closely spaced pressure sensors can be used to approximate the complex intensity and its curl.

Figure 1(c) shows the particle paths corresponding to equally spaced range points at the 20 m depth, shown by the white dots in Figs. 1(a) and 1(b). The particle motion ranges from linear in regions of constructive interference, to elliptical in regions of destructive interference. The direction of particle motion along these paths is indicated by the sign of vorticity. For a (+) sign of active intensity vorticity, the polarization is counter-clockwise; for a (−) sign, the polarization is clockwise. The polarization of the particle motion on either side of a destructive or constructive interference contour is opposite. (These contours are indicated by the white lines in Fig. 1(a), the sign of active intensity vorticity is the same between these contours and is indicated by the (+/−) symbol.)

The vector intensity properties discussed in the steady-state field also occur for time-dependent pulses. To simplify analysis of the active intensity field in shallow water waveguides, we can take advantage of the bandwidth of a pulse and truncate the measured time-series to limit the number of interfering reflections. For example, before the onset of interference from the bottom reflection, the field of a pulse generated by a near-surface source will show a similar destructive interference pattern to that depicted in Fig 1.

Figure 2(a-c) shows, at three sequential times, the active intensity magnitude (normalized to the magnitude at 1 m range) of a 2 ms duration pulse centered at frequency 1000 Hz with source depth equal to 1.5 m. A destructive node propagating along the wavefront follows a node-line (dashed line) which corresponds to a minimum of the Lloyd mirror pattern shown in Fig. 1. On either side of this node-line, the active intensity vorticity has a different sign (and particle motion polarization flips.) The simulated pulse in Fig. 2 is constructed from a Fourier synthesis of narrowband parabolic equation (PE) simulations over a 500 Hz bandwidth. The environmental model used in the PE simulations is based on the SW06 waveguide, described in detail in section 3.

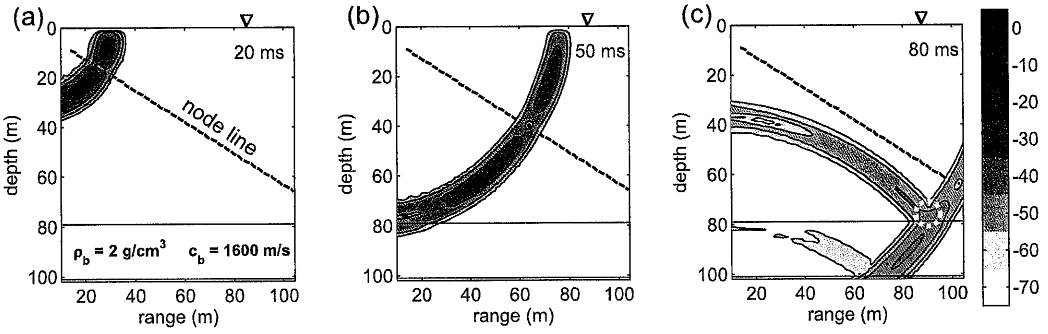

Figure 2: Three sequential snapshots of the active intensity magnitude contours in log scale (relative to the maximum at 1 m). The dotted node line corresponds to the minimum due to destructive interference of the direct and surface reflected paths. The white dotted region is analyzed in Fig 3.

The formation of a vortex in active intensity can occur when the acoustic field undergoes a complete cancellation, forming a null or dislocation in the field. This cancellation occurs when there are opposing energy fluxes, such as those from the sea-surface and sea-floor reflections; the specific vortex structures are centered at points where both the acoustic particle velocity field and pressure are zero. Vortex formation first occurs near the sea-floor where there is interference between opposing energy fluxes from the direct (and surface reflected) path and its subsequent seabed reflected path. The white dotted circle in Fig. 2(c) identifies a region containing a vortex.

2.2 ACTIVE AND REACTIVE INTENSITY IN A VORTEX REGION

The vortex feature identified by the white dotted circle in Fig. 2(c) provides a useful demonstration for additional focus on intensity properties, in particular the relationship between active intensity vorticity and reactive intensity. Figure 3(a) shows an expansion of this region along with the vector field indicating the direction of the active intensity vector. The active intensity contours correspond to the same magnitude scale in Fig. 2 (normalized by the intensity magnitude at 1 m range.)

Some additional insights into the relationship between the active intensity vector field and the curl can be shown by an application of Stokes theorem. Stokes theorem applied to the active intensity vector field is

$$\iint_A \boldsymbol{n} \cdot (\nabla \times \vec{\boldsymbol{I}})\, da = \oint_C \vec{\boldsymbol{I}} \cdot dR \tag{5}$$

and states that the average vorticity in a particular region (the surface integral on the left) can be determined by integration along a closed circuit (the contour integral on the right). Although Eq. (4) can be used to directly measure the active intensity vorticity at a point, direct measurement by pressure sensors is much more complicated, and the right side of Eq. (5) provides an easier way to measure the active intensity vorticity. Furthermore, it provides an intuitive interpretation of the average vorticity (and more clearly its sign) from vector field plots like Fig. 3. This is particularly useful when attempting to identify a vortex feature, which is characterized by a sign change.

For example, selecting two rectangular paths, labeled A and B in Fig. 3, that each have one horizontal edge passing through the minimum at 77.5 depth, we can demonstrate this sign change above and below a null. The magnitude of the field along this edge is minimal, and moreover its direction is

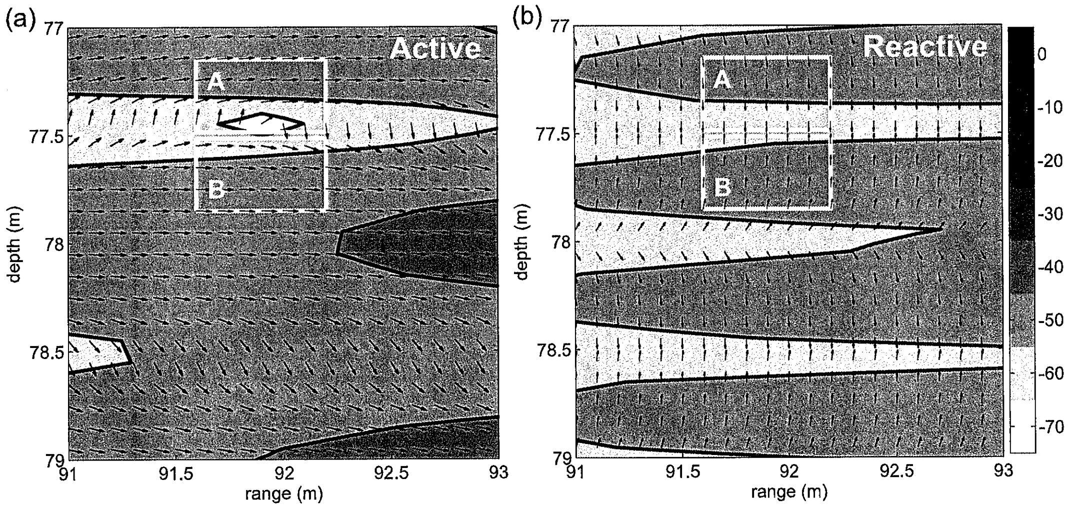

Figure 3: (a) Contours of the active intensity magnitude and the direction of the active intensity vector field of the white dotted region in Fig. 2(c) Boxes A and B highlight regions where vorticity is of opposite sign. (b) Contours of the reactive intensity magnitude and the direction of the reactive intensity vector field. Both (a) and (b) are normalized by the active intensity magnitude 1 m from the source.

perpendicular to the contour; this edge contributes very little to either contour integral. Integrating clockwise along path A above the null, the vectors along the other three sides are more or less in the direction of integration. All three sides add together and the active intensity vorticity is positive. Integrating clockwise along path B, below the null, the vectors point in the opposite to the direction of integration; the active intensity vorticity is negative.

Reactive intensity can be exploited to detect vortex features from two vertically spaced hydrophones. Figure 3(b) shows the direction of the reactive intensity vector plotted over contours of the reactive intensity magnitude (normalized by the active intensity magnitude at 1 m range.) Note the sign of active intensity vorticity corresponds to the direction of the reactive intensity, the boxes A and B correspond to the same region as those in Fig. 3(a).

We can use the phase relationship between the vertical and horizontal particle velocities described in Eq. 4 to clarify the relationship between vertical reactive intensity and active intensity vorticity. As Fig. 3(b) shows, the reactive intensity vector is predominately in the vertical direction. Since there is no horizontal reactive intensity, the horizontal particle velocity and pressure are in phase; the phase of the pressure signal can be substituted for the phase of the horizontal particle velocity in Eq. 4. The out-of phase component of pressure and vertical particle velocity (which is Q_z) is proportional to the active intensity vorticity. Therefore, the sign of Q_z and active intensity vorticity are the same.

A defining feature of the vortex structure is that about the null in the pressure magnitude, the active intensity vectors are aligned head-to-tail. As a vector field must pass through a null before changing sign, the active intensity switches directions at the second null, the saddle-point, where the pressure magnitude and reactive intensity are non-zero. Note that over a small vertical distance ($\sim \lambda/100$) between the two active intensity nulls, the sign of Q_z and active intensity vorticity are opposite. This only occurs in a vortex region close to the vortex center, in general the signs of Q_z and active intensity vorticity are the same.

3 EXPERIMENTAL OBSERVATIONS

Interpretation of a set of acoustic observations from the 2006 Shallow Water Experiment (SW06) central site in terms of the vector intensity can lead to additional insights on geo-acoustic properties. The experimental data presented here consists of pressure measurements from vertically spaced hydrophones (20 cm separation) centered at depth 50 m on a moored hydrophone array, location 39.0245 N, 73.0377 W. An acoustic transducer is towed at 75 m depth from the stern of the R/V KNORR to produce a series of 1000 Hz pulses of 2-3 ms duration. The transducer pulses every 12 s as the R/V KNORR moves outward from the receiver at 0.1 m/s from 50-300 m range.

Due to the proximity of the seabed (depth 79 m), the first arrival consists of a direct and bottom reflected path. This interaction produces an active intensity vorticity similar to the example discussed previously in Fig. 2. Depending on the source/receiver range, a reflection from a sub-bottom layer is observable in the data. Extensive geo-acoustic modeling and surveying, summarized in Jiang, et. al [4], has identified a bottom model consisting of a high speed basement (~1740 m/s), the R-reflector, located 22 m below a lower-speed sediment layer (~1600 m/s). The bathemetry of the SW06 central site can be regarded as flat. We show here that reflections from this sub-bottom layer are clearly observable in the vertical intensity measurements.

To compute the complex vertical intensity from the pressure measurements, an estimate of the vertical particle velocity is first formulated by

$$\vec{v}(t) = -\int_0^t \frac{\nabla p(t')}{\rho_0} dt' \tag{6}$$

where the finite-difference of the two pressure channels is used to approximate the pressure gradient. The complex vertical intensity in Eq. (1) is formulated by a complex representation of vertical particle velocity and pressure, i.e. their Hilbert-transform pairs; see [5] for a detailed description of this complex intensity formulation from real pressure measurements and discussion of measurement errors associated with this technique.

The vertical reactive intensity (Q_z, used here as a surrogate of active intensity vorticity) responds to the interference of the first-arrival and sub-bottom arrival. The sign of the vertical reactive intensity, as well as the particle motion polarization and active intensity vorticity, change as a function of range.

Importantly, the range dependence of the Q_z change-in-sign is related to the sediment properties. PE simulations of the pressure and particle velocity fields are used to demonstrate the effect of the reflection process on the vector intensity field. The SW06 bottom model used in these simulations (and used for the shallow source simulations in Figs. 2-3) consists of a water-column depth of 79 m with a sound-speed profile (directly measured), a sediment layer 22 m thick with c_{sed} = 1600 m/s and ρ_{sed} = 2000 kg/m^3, and a sub-bottom basement layer modeled as a half-space with c_R = 1740 m/s and ρ_R = 2200 kg/m^3. Sediment attenuation, documented in Choi, et. al [6], of the top sediment layer is 0.05 dB/m/kHz and 0.3 dB/m/kHz for the R-reflector sub-bottom basement.

3.1 PULSE PROPAGATION

To demonstrate the effect of the bottom model on these simulated pulses, we first simulate a 2-ms pulse with a half-space model. The bottom half-space model properties are ρ_{sed} = 2000 kg/m^3 and c_{sed} = 1600 m/s with an attenuation of 0.05 dB/m/kHz, representative of top layer of the SW06 environment without the R-reflector component. Figure 4(a) shows the sound speed profile with the sediment interface at 79 m and the first three ray paths, arriving in order direct, bottom and surface. Narrow-band simulations of pressure and particle velocity are computed over the frequency range 500-1500 Hz are computed with the PE code with the resulting fields converted into time series by Fourier synthesis.

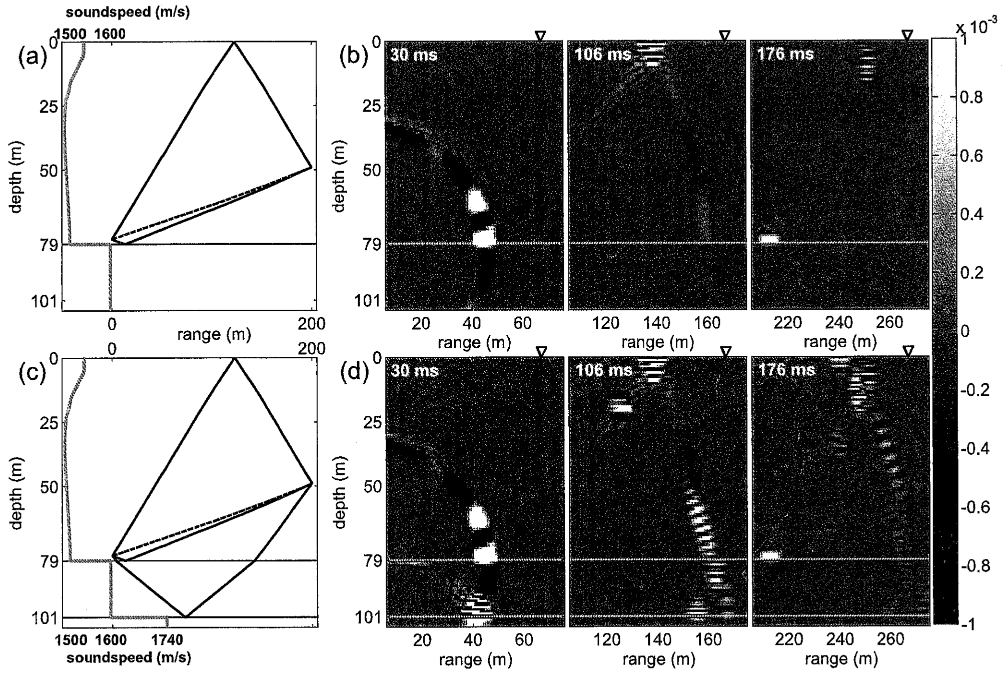

Figure 4: (a) The SW06 sound speed profile and half-space bottom model showing the first three eigenrays. (b) Three snapshots of the vertical reactive intensity for a 2-ms PE simulated pulse at 1000 Hz emanating from a source at 75 m depth, computed using the half-space model. (c) The full SW06 bottom model and first four eigenrays. (b) Three snapshots of the vertical reactive intensity for a 2-ms PE simulated pulse at 1000 Hz emanating from a source at 75 m depth, computed using the layered bottom model.

Figure 4(b) shows three snapshots of the vertical reactive intensity field as the pulse propagates down the waveguide for the half-space model in Fig. 4(a). Due to the relative proximity of the source to the sea-floor ($d/\lambda \sim 1$), the field along the wavefront is similar to the Lloyd Mirror pattern demonstration of a near surface source in Fig. 2. Nodes of destructive interference follow the node-lines predicted by the interference pattern of the source and its image; on either side of this node line the vertical reactive intensity changes sign, indicating a sign change in active intensity vorticity and particle motion polarization.

When the R-reflector 22 m below the sea-floor is included in the bottom model, the interference between the bottom and sub-bottom reflected paths manifests an interference pattern observable on the direct arrival. Figure 4(c) shows the sound speed profile used in the PE simulation including the R-reflector at 101 m depth and an additional ray reflecting from this layer. Figure 4(d) shows the pulse at the same three instances for this bottom model. When the reflection from the sub-bottom R-reflector and the direct arrival overlap, the interference causes additional banding compared to that caused by the interference of the direct and bottom arrivals alone (as seen in the half space model in Fig. 4(b).) Again, the banding corresponds to change in sign of active intensity vorticity, or particle motion polarization. An important property of this banding is that it corresponds to the angular difference of the direct and R-reflected arrival angles.

3.2 COMPARISON OF EXPERIMENTAL AND MODEL RESULTS

The experimental data consists of alternating 2 and 3 ms truncated sinusoidal pulses centered at frequency 1000 Hz. A GPS location measured for each pulse (separated roughly every 12 seconds) is used to plot the complex intensity at the 50 m receiver depth as a function of time and range from 50 to 300 m. The effect of the sub-bottom layer is clearly observable by time-aligning the experimental data. Figure 5(a) shows the experimentally measured pressure magnitude squared (in log scale, normalized to the maximum measured $|p|^2$ at range 50 m) and Figs. 5(b) and 5(c) the vertical active and reactive intensities normalized by the maximum value of $|p|^2/\rho_0 c$ at 50 m. Time-aligned PE simulated time-series at the 50 m receiver depth from the simulation used in Fig. 4(c-d) are plotted alongside the experimental data and are normalized in the same fashion as the experimental data.

Due to the alternating 2 and 3 ms experimental pulses, the source fluctuation adds a degree of variance in the pressure squared measurements. While the two arrivals are time-separated the arrival

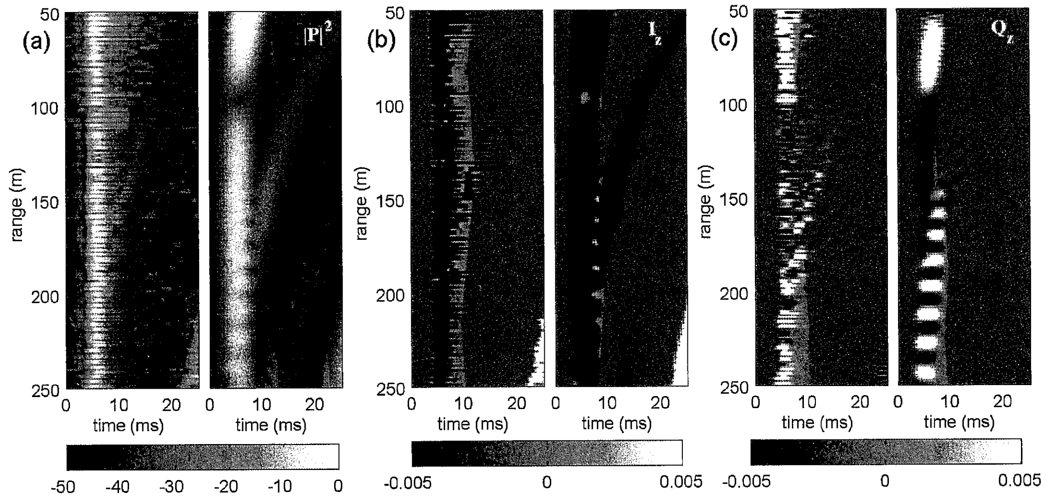

Figure 5: Experimental measurements at 50 m depth of (a) pressure magnitude squared divided by $\rho_0 c$, (b) vertical active intensity and (c) reactive intensity (all normalized by the maximum $|p|^2/\rho_0 c$ at 50 m) are plotted next to their respective PE simulated data (see Fig. 4(c) for the environmental model.)

structure can be used to determine bottom properties; however, this method is confounded when the arrivals are coincident. As Fig. 5(b) shows, at ranges greater than 120 m, the vertical active intensity is sensitive to the interference from a sub-bottom arrival (an arrival from below corresponds to a negative energy flux). The periodic switching from negative to positive when there is strong destructive interference appears as white dots on the main arrival. Note that both the data and simulation show a second sub-bottom arrival (around range 210 m and time 15 ms) that arrives before the surface arrival at 24 ms; this second sub-bottom path corresponds to a bottom path reflected internally, reflecting from the sub-bottom layer twice.

As Fig 5(c) shows, the vertical reactive intensity provides the clearest measure to study the interaction of two coincident wavefronts. The vertical reactive intensity exhibits a banding of positive and negative values, changing sign roughly every 8.5 m. This range step is in agreement with the estimates from the PE simulations of the SW06 bottom-model. The range dependence of the sign-change is dependent on the angular difference of the incoming wavefronts, a property effected by the sediment sound-speed of the top layer. A bottom model underestimating the sound-speed of the top-layer by 50 m/s increases the range step to 13 m, a model overestimating the top-layer sound speed by 50 m/s decreases the range step to about 6 m. This change in range step is due to the energy reflected from the bottom layer and propagating near the critical angle of the top sediment layer; changing the critical angle changes the angular difference of the two arrivals. A change in sound-speed also effects the arrival time of the sub-bottom reflection. The correct bottom model for this comparative analysis suggests a sediment sound-speed at, or slightly below, 1600 m/s, a value in close agreement with the observations summarized in [4].

This vertical reactive intensity estimate of angular difference is stable in regards to fluctuations in the source level. A notable source of variability is the fluctuation in the source depth caused by ship heave. This effects the banding of the direct and first bottom-reflected arrival, the feature present in both Figs. 4(b) and 4(d), since the angular difference of these two arrival angles is very small. However, the range step (8.5 m) associated with the interference of the direct arrival and the sub-bottom arrival, as shown in Fig. 4(d), is not effected by source depth fluctuation. The difference between these two arrival angles is dependent on the bottom properties and changes very little with source depth fluctuation.

4 SUMMARY AND CONCLUSION

The formulation of complex intensity from acoustic measurements reveals properties of the interference between multiple coherent arrivals. In a waveguide, reflections from the boundaries cause active intensity vorticity, a property of the intensity field that corresponds to the elliptical particle motion and the particle motion polarization. In a waveguide with horizontal boundaries, the vertical reactive intensity indicates the vorticity features of active intensity. The experimental data presented focuses on the interference of reflections from sub-bottom layers in an ocean waveguide. The example detailed here uses both experimental and synthetic data to demonstrate the stability of complex intensity properties, and how to infer these vector properties from a single vertical component of intensity.

The spatial structure of the active intensity vorticity is related to the both the source-receiver geometry and geo-acoustic properties. Although only the vertical component is analyzed here over a limited bandwidth due to constraints on the hydrophone finite-difference technique, properties of the active intensity can be measured at a point by using tri-axial vector sensor technology. Measurement of the active intensity vorticity (or particle motion path) provides a tool for analysis of interference fields beyond analysis of pressure-magnitude fluctuations. This view of the acoustic field is not dependent on source amplitude and is stable in relation to source depth fluctuations.

ACKNOWLEDGMENTS

This work is supported by the Office of Naval Research (ONR) Ocean Acoustics Program (Dahl) and the ONR Graduate Trainee Fellowship (Dall'Osto).

REFERENCES

1. Shchurov, V.A., V.P. Kuleshov and A.V. Cherkasov, "Vortex Properties of the Acoustic Intensity Vector in a Shallow Sea," Acoustical Physics, 2011 Vol. 57 No. 6 pp 851-856 (2011).
2. D'Spain, G.L., J.C. Luby, G.R. Wilson, and R.A. Gramann, "Vector sensors and vector sensor line arrays: Comments on optimal array gain and detection," J. Acoust. Soc. Am. 120 171 (2006).
3. J.A. Mann III, J. Tichy, and A.J. Romano, "Instantaneous and time averaged energy transfer in acoustic fields." J. Acoust. Soc. Am. 82, p. 17 (1987).
4. Jiang, Y.M., N.R. Chapman, P. Gerstoft, "Estimation of Geo-acoustic Properties of Marine Sediment Using a Hybrid Differential Evolution Inversion Method." IEEE J. Oceanic Engineering, Vol 35, No. 1, January (2010).
5. Dall'Osto, D.R., P.H. Dahl, and J.W. Choi, "Properties of the acoustic intensity vector field in a shallow water waveguide," J. Acoust. Soc. Am. 131(3): 2023-35 (2012).
6. Choi, J. W., Dahl, P. H., Goff, J. A, "Observations of the R reflector and sediment interface reflection at the Shallow Water '06 Central Site." J. Acoust. Soc. Am., Vol. 124, No. 3, EL128 (2008).